energies

MDPI

Article

Analysis and Design of a Multi-Resonant Circuit for Applications of Wireless Capacitive Power Transmission

Eduardo Salvador Estevez-Encarnacion [1], Leobardo Hernandez-Gonzalez [1,*], Juan C. Sanchez-Garcia [1], Jazmin Ramirez-Hernandez [1,*], Domingo Cortes [1], Mario Ponce-Silva [2] and Oswaldo Ulises Juarez-Sandoval [1]

[1] Escuela Superior de Ingeniería Mecánica y Eléctrica, Unidad Culhuacan, Instituto Politécnico Nacional, Av. Santa Ana No. 1000, Col. San Francisco Culhuacan, Mexico City 04430, Mexico; eesteveze1400@alumno.ipn.mx (E.S.E.-E.); jcsanche@ipn.mx (J.C.S.-G.); domingo.cortes@gmail.com (D.C.); ojuarezs@ipn.mx (O.U.J.-S.)

[2] Tecnológico Nacional de México—CENIDET, Interior Internado Palmira s/n, Col. Palmira, Cuernavaca 62490, Mexico; mario.ps@cenidet.tecnm.mx

* Correspondence: lhernandezg@ipn.mx (L.H.-G.); jramirezhe@ipn.mx (J.R.-H.)

Abstract: Capacitive technology for wireless power transmission has been shown to be a good option for charging the batteries of electric vehicles. It offers better coupling between the transmitter and the receiver than inductive power transmission. On the other hand, it has some disadvantages; for example, it is very sensitive to the distance between plates. Several ideas have recently been proposed to overcome this disadvantage. However, a proper analysis methodology is still lacking, as is a proper design procedure for the circuits used in capacitive transmission. In this paper, an analysis and design methodology is presented for applying the Z-tank resonant circuit to capacitive power transmission, and the theoretical design methodology is based on normalized equations with respect to the operating resonance frequency. The analysis methodology and design procedure result in a circuit where the resonance frequency remains constant despite changes in the distance between the capacitive plates. The simulation results validate the proposal; to ensure robust, realistic simulation results, parasitic elements were considered in all reactive components, and robust models were built for the switching elements, such as MOSFETs and diodes. The results show that the multi-resonant characteristic of the circuit achieves maximum energy transfer and high efficiency.

Keywords: multi-resonant circuits; CPT; LCLC circuit

Citation: Estevez-Encarnacion, E.S.; Hernandez-Gonzalez, L.; Sanchez-Garcia, J.C.; Ramirez-Hernandez, J.; Cortes, D.; Ponce-Silva, M.; Juarez-Sandoval, O.U. Analysis and Design of a Multi-Resonant Circuit for Applications of Wireless Capacitive Power Transmission. *Energies* **2022**, *15*, 2252. https://doi.org/10.3390/en15062252

Academic Editors: Mauro Feliziani and Alon Kuperman

Received: 27 January 2022
Accepted: 16 March 2022
Published: 19 March 2022

1. Introduction

Capacitive power transmission (CPT) is commonly applied in different technologies, for example, medical equipment, electronic equipment, transportation battery recharging, and home appliances [1–6]. CPT technology transfers electric power through plates that generate an electric field. It presents advantages compared to inductive power transmission (IPT) [7–9], such as lower cost, a reduction in the dispersion of Eddy currents, a lack of susceptibility to external factors, and the fact that it is unaffected by liquids.

To transfer energy between metal plates, [10] proposes a scheme that uses a two-plate coupling interface on the primary side and has an inductor on a secondary coil to receive the transferred power. In [11], the authors present a single-wire scheme that uses one pair of coupling plates instead of a traditional design with two pairs, thus allowing for a larger variation in the distance between plates. In [12], a CPT system with an F-type compensation circuit is used to reduce the stress on the inverter semiconductor devices when energy moves through the plates.

CPT systems are also included in various high-power applications and are already being employed in electric vehicle charging. In [13], an LCLC compensation circuit in a CPT scheme is presented in a 2.4 kW prototype with an efficiency of 90.8%; in [14], a CLLC

compensation circuit in a 2.57 kW prototype with an efficiency of 89.3% is presented. In [15], a six-plate topology is used to reduce the radiation loss, allowing for a power transfer with an efficiency of 91.6% in a 1.97 kW prototype. In [16], the authors present a near-field phased array that is properly distributed with a cancellation scheme in order to obtain a high power-density, thus achieving a radiation loss reduction. In [17], a multi-modular CPT system uses the parasitic capacitance between the plates to achieve a high-performance, high-power system. In [18], the authors describe a design methodology that uses double-sided LC compensation in the system and takes inductance detuning into consideration. Removing the inductance allows for a soft-switching operation in the converter, thereby reducing stress on the semiconductor devices.

Although the research discussed above forms the basis for the analysis and design of CPT systems, in practical applications, the coupling between capacitive plates is still a problem. Since the energy transfer takes place through the air and its dielectric value is small, the capacitance is just a few tens of picofarads when the distance increases. Therefore, it is necessary to raise the voltage and the resonance frequency on the coupling capacitance to achieve a high-power transfer. Furthermore, the CPT system is sensitive to parameter changes due to the high value of its quality factor, Q. For these reasons, further research is necessary to establish a systematic method of analysis, achieve the reduction in voltage stress, determine the optimal load impedance, and reduce the impact of operating frequency changes on energy transmission efficiency [19,20].

Some topologies have been proposed to compensate for the resonant frequency. Among these topologies are LCLC, LCL, and LC; in particular, it has been shown that a double-sided CL compensation grid can be used to achieve a high-power energy transfer and long-distance variation and to simplify the compensation circuit [21–23]. It also has been found that in the same way as in IPT applications, in CPT there is also an optimal load to ensure maximum power transfer. However, a systematic design procedure for this compensation method is still lacking.

In this paper, an analysis methodology and a systematic procedure for using a modified Z-multi-resonant circuit in capacitive wireless power transmission are presented. The proposed design is based on normalized graphs that allow for calculating the parameters of the compensation circuit for maximum energy transfer.

This paper is organized as follows: In Section 2, the problem to be solved is described. The proposed method for multi-resonant circuit analysis is presented in Section 3. In Section 4, our proposal for a design procedure is presented. In Section 5, the simulation results that validate the design methodology are presented. Finally, the conclusions are presented in Section 6.

2. Capacitive Wireless Transmitter

Although there have been significant advances in the research on wireless charging systems with capacitive coupling, the technology is certainly still behind that based on inductive coupling. In capacitive coupling, energy is transferred through an electric field between capacitive plates; the energy transfer happens without electromagnetic radiation.

Figure 1 shows a block diagram of a capacitive power transmitter. One of the biggest problems with this device is the high dependence of its resonance frequency (f_0) on the distance between the capacitive plates. In this type of resonant circuit, distance (d) between plates modifies the resonance frequency according to Expression (1):

$$f_0 = \frac{1}{\sqrt{L \cdot C_{plates}}} \tag{1}$$

A solution to the high dependence of f_0 on d is to replace the resonant circuit with a multi-resonant circuit. This multi-resonant circuit, also called a stabilization circuit, aims to keep f_0 constant even when the distance between the capacitive plates changes.

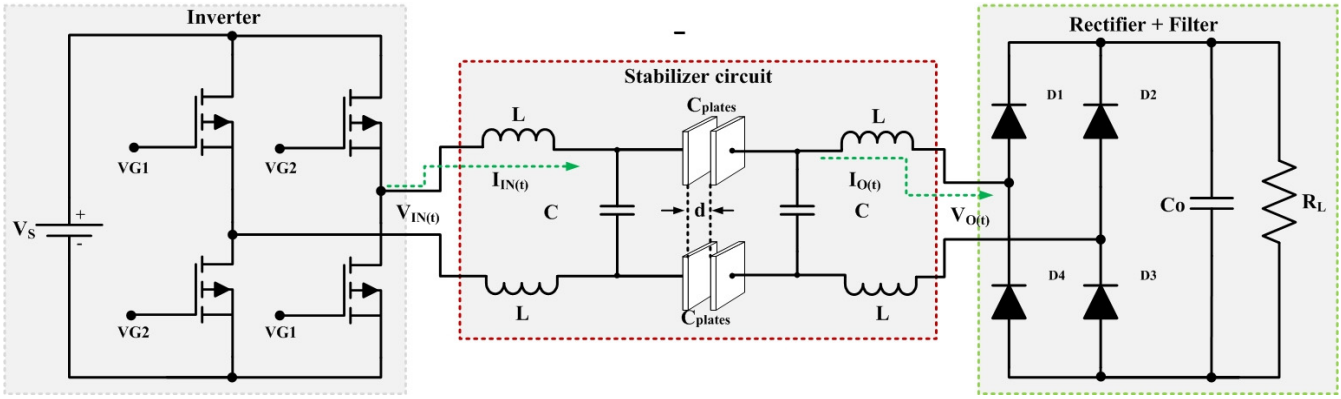

Figure 1. Circuit with capacitive power transfer.

Several multi-resonant circuits have been described [24]; however, their use is limited by the design complexity and the lack of an appropriate methodology for determining the values of the components that ensure the maximum power transfer and high resonance frequency stability. In this paper, we propose a multi-resonant circuit analysis and a design methodology for integrating the multi-resonant circuit into the capacitive wireless transmitter without these limitations.

3. Proposed Multi-Resonant Circuit

The multi-resonant circuits are composed of a combination of three or more reactive components, such as inductors and capacitors. As a result, one of their most important characteristics is the capacity to produce more than two resonance frequencies; stated another way, the interconnection among reactive components results in several characteristics based on impedance, voltage, and current, thus rendering the circuits suitable for use in different applications.

In [24], thirty-six multi-resonant circuits with three components are proposed, with an analysis of each one in the context of the wireless power transfer application based on capacitive coupling and considering a voltage source as input. All of them satisfied two conditions:

- The capacitors must not be connected in parallel to the voltage source;
- One capacitor must be connected in series to the output.

Considering these conditions, only two multi-resonant circuits from the thirty-six mentioned in [24] are feasible for CPT applications. Their configurations are shown in Figure 2.

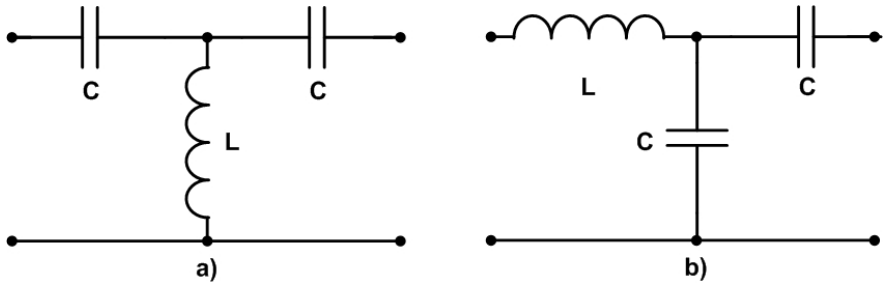

Figure 2. Feasible multi-resonant circuits for CPT system applications: (**a**) X-Tank; (**b**) Z-Tank.

In this paper, in order to achieve a frequency compensation due to coupling capacitance changes, the Z-tank of Figure 2b is modified as shown in Figure 3.

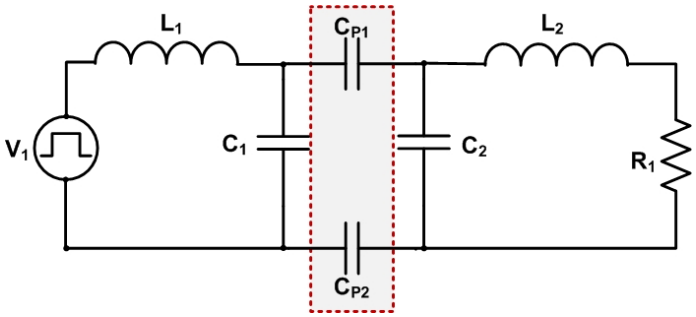

Figure 3. Z-Tank modified.

Figure 4 shows the equivalent circuit where C_2, L_2, and R_1 are regrouped in Z_2; C_{p1} and C_{p2} are now in series. To enable the analysis of the modified multi-resonant circuit shown in Figure 4 and to obtain a design methodology, we propose the use of an equivalent circuit where coupled capacitors C_{p1} and C_{p2} are represented by an equivalent capacitor C_{eq}, as shown in Figure 5. From this figure, it can be observed that C_{eq} is given by:

$$C_{eq} = \frac{C_{p1} \cdot C_{p2}}{C_{p1} + C_{p2}} \tag{2}$$

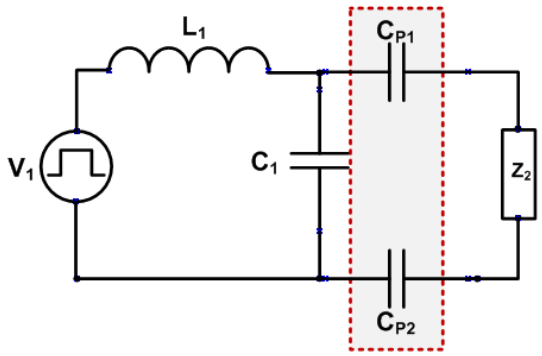

Figure 4. Equivalent circuit of Z-Tank modified.

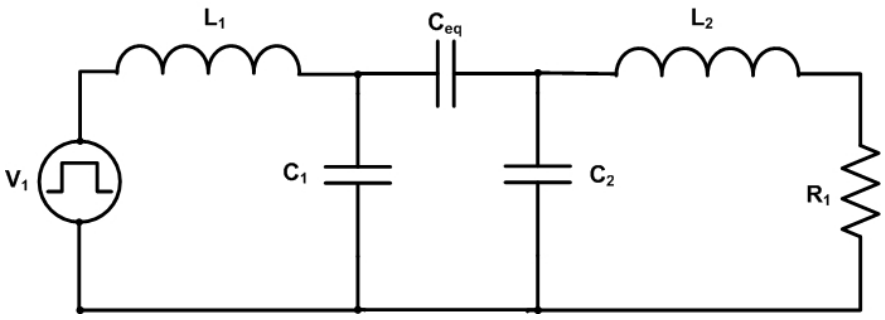

Figure 5. Equivalent Z-Tank modified.

Considering $C_p = C_{p1} = C_{p2}$, Expression (2) can be rewritten as:

$$C_{eq} = \frac{C_{p1} \cdot C_{p2}}{C_{p1} + C_{p2}} = \frac{C_p^2}{2 \cdot C_p} = \frac{C_p}{2} \tag{3}$$

4. Modified Multi-Resonant Z-Tank Design

For the multi-resonant circuit design, a theoretical analysis of the total impedance (Z_T), the total voltage gain (G_{VT}), and the total current gain (G_{IT}) is performed to obtain

normalized graphs. Having a normalized graph allows us to determine the conditions of maximum energy transfer regardless of the value of its elements.

The following conditions are considered for the analysis:

- $C = C_1 = C_2$;
- $L = L_1 = L_2$;
- A relationship "m" between capacitances is proposed: $m = \frac{C}{C_{eq}}$;
- All graphs will be based on the absolute value of the obtained expressions.

4.1. Impedance Analysis

The impedance analysis is performed using a series–parallel reduction in the circuit in Figure 5, as shown in Figure 6.

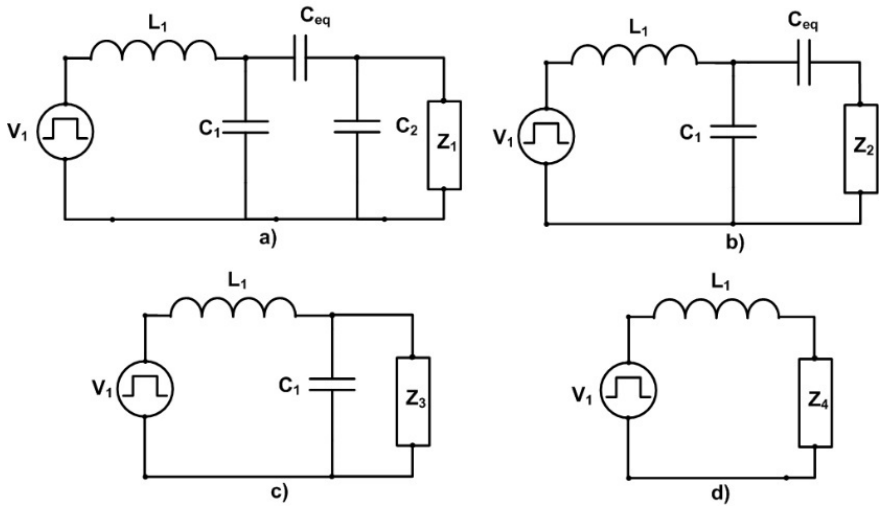

Figure 6. Modified Z circuit reduction process: (**a**) Equivalent Z-Tank modified; (**b**) Z_1 and C_2 in parallel are reduced to Z_2; (**c**) C_{eq} and Z_2 in series are reduced to Z_3; (**d**) C_1 and Z_3 in parallel are reduced to Z_4.

From Figure 6, expressions for Z_1, Z_2, Z_3, Z_4, and Z_T can be obtained through FHA (First Harmonic Approximation) analysis, where the network is analyzed only for the first harmonic:

$$Z_1 = R_1 + XL_2 = R + sL \tag{4}$$

$$Z_2 = Z_1 \left|\left| X_{C_2} = Z_1 \right|\right| \frac{1}{sC} = \frac{sL + R}{s^2LC + sRC + 1} \tag{5}$$

$$Z_3 = Z_2 + X_{C_{eq}} = Z_2 + \frac{1}{s\frac{C}{m}} \tag{6}$$

$$Z_3 = \frac{s^2LC[m+1] + sRC[m+1] + m}{sC(s^2LC + sRC + 1)} \tag{7}$$

$$Z_4 = Z_3 \left|\left| X_{C_1} = Z_3 \right|\right| \frac{1}{sC} \tag{8}$$

$$Z_4 = \frac{s^2LC[m+1] + sRC[m+1] + m}{sC(s^2LC[m+2] + sRC[m+2] + [m+1])} \tag{9}$$

$$Z_T = Z_4 + X_{L_1} = Z_4 + sL \tag{10}$$

To facilitate the analysis and obtain normalized expressions, the following relationships are defined:

- γ = Normalized resonance frequency $\left(\frac{f_{operation}}{f_{resonance}}\right)$;

- ϕ = Normalized cut-off frequency $\left(\frac{f_{operation}}{f_{cut-off-RC}}\right)$;
- ω = Angular frequency $(2\pi f_{operation})$.

To obtain a normalized graph, Z_T is rewritten as:

$$Z_T = \frac{\gamma^4[m+2] - 2\gamma^2[m+1] + m + j\phi\{[m+1] - \gamma^2[m+2]\}}{j\omega C([m+1] - \gamma^2[m+2] + j\phi[m+2])} \tag{11}$$

Impedance Z_T can be expressed as:

$$Z_T = X_c Z_{nor} \tag{12}$$

where

$$X_C = \frac{1}{j\omega C} \tag{13}$$

$$Z_{nor} = \frac{\gamma^4[m+2] - 2\gamma^2[m+1] + m + j\phi\{[m+1] - \gamma^2[m+2]\}}{[m+1] - \gamma^2[m+2] + j\phi[m+2]} \tag{14}$$

Because both the numerator and denominator of Expression (14) are complex expressions, we propose obtaining the magnitude of both expressions as follows:

$$|Z_{nor}| = \frac{\sqrt{(\gamma^4[m+2] - 2\gamma^2[m+1] + m)^2 + \phi^2([m+1] - \gamma^2[m+2])^2}}{\sqrt{([m+1] - \gamma^2[m+2])^2 + \phi^2[m+2]^2}} \tag{15}$$

Figure 7 shows the graph corresponding to Expression (15), where γ is a vector with a range from 0.5 to 1.5, ϕ is a vector with a range from 0 to 0.1, and m = 50. It can be observed that the magnitude of the normalized impedance is near 0 when working near resonance (γ = 1) regardless of the value of φ. If γ slightly decreases from 1 and ϕ = 0, then Z_T reaches its maximum value, but if $\phi > 0$, then Z_T decreases to 0. As a result of this observation, it can be concluded that the value of $|X_C|$must be large to compensate for the normalized impedance magnitude so that the total impedance does not affect the circuit efficiency.

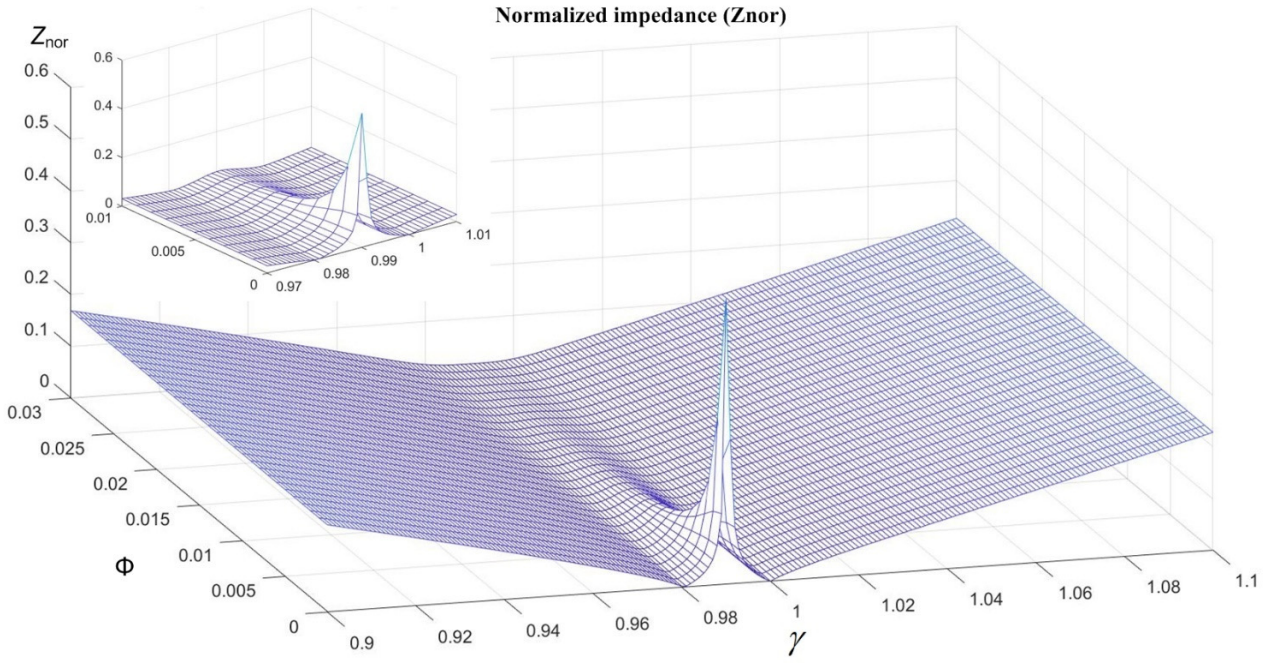

Figure 7. Normalized impedance in the function of γ, ϕ, and m = 50.

To increase X_C, ω or C should decrease; however, at a low frequency, this is not a good alternative as it would increase both the value of plate capacitance and conduction losses. As a result, we now analyze the optimal operating frequency for working with low capacitance values.

4.2. Resonance Frequency Analysis

In [25], it is mentioned that, if the parallel capacitors are larger than the coupling capacitor, the parallel capacitors will dominate the resonance frequency. However, the authors do not indicate how much greater this relationship should be. To find the optimal ratio value from Expression (11), the behavior of Expressions (16)–(18) is analyzed:

$$\gamma^4[m+2] \tag{16}$$

$$\gamma^2[m+1] \tag{17}$$

$$\gamma^2[m+2] \tag{18}$$

Considering that operation in the resonance frequency is a requirement, the value of γ needs to be 1. In Expressions (16)–(18), γ is multiplied by different factors; therefore, the approximation error is analyzed when Expressions (16)–(18) are equal to the relation with m according to:

$$\gamma = \sqrt[4]{\frac{m}{m+2}} \approx \sqrt{\frac{m}{m+1}} \approx \sqrt{\frac{m}{m+2}} \tag{19}$$

Table 1 shows a comparison of the values obtained with Expressions (16)–(18) by using γ = 1 for different values of m.

Table 1. Behavior of Expressions (16)–(18) with γ = 1 with different "m" values.

M	$\sqrt[4]{\frac{m}{m+2}}$ (a)	$\sqrt{\frac{m}{m+1}}$ (b)	$\sqrt{\frac{m}{m+2}}$ (c)	%Error		
				(a) Vs γ	(b) Vs γ	(c) Vs γ
10	0.9554	0.9535	0.9129	4.46%	4.65%	8.71%
20	0.9765	0.9759	0.9535	2.35%	2.41%	4.65%
30	0.9840	0.9837	0.9682	1.60%	1.63%	3.18%
40	0.9879	0.9877	0.9759	1.21%	1.23%	2.41%
50	0.9902	0.9901	0.9806	0.98%	0.99%	1.94%
60	0.9918	0.9918	0.9837	0.82%	0.82%	1.63%
70	0.9930	0.9929	0.9860	0.70%	0.71%	1.40%
80	0.9938	0.9938	0.9877	0.62%	0.62%	1.23%
90	0.9945	0.9945	0.9891	0.55%	0.55%	1.09%
100	0.9951	0.9950	0.9901	0.49%	0.50%	0.99%

The normalized resonance frequency approaches 1 when the value of m increases, and for values of $m \geq 50$, the approximation error in Expressions (16)–(18) is below 1%, so it can be concluded that working with a value of m = 50 allows for a proper stabilization of the resonance frequency. Expression (16) has the lowest error rate, so it is used for future calculations.

4.3. Voltage Gain Analysis

To obtain the voltage gain expression (G_V), the voltage divisor method and the expressions obtained in the impedance analysis are used; the resulting expression is shown in Expression (20). However, since magnitude is required to obtain a normalized graph, the expression used is shown in Expression (21):

$$G_V = \frac{j\phi}{\gamma^4[m+2] - 2\gamma^2[m+1] + m + j\phi\{[m+1] - \gamma^2[m+2]\}} \tag{20}$$

$$|G_V| = \frac{\phi}{\sqrt{(\gamma^4[m+2] - 2\gamma^2[m+1] + m)^2 + \phi^2([m+1] - \gamma^2[m+2])^2}} \quad (21)$$

The normalized graph for $|G_{VT}|$is shown in Figure 8; the magnitude increases when the variable ϕ moves away from 0 and γ tends to 1. The multi-resonance effect can be observed when ϕ is near to 0, where a second resonance peak appears beside the original resonance peak. Therefore, this type of compensation circuit presents a multi-resonance effect.

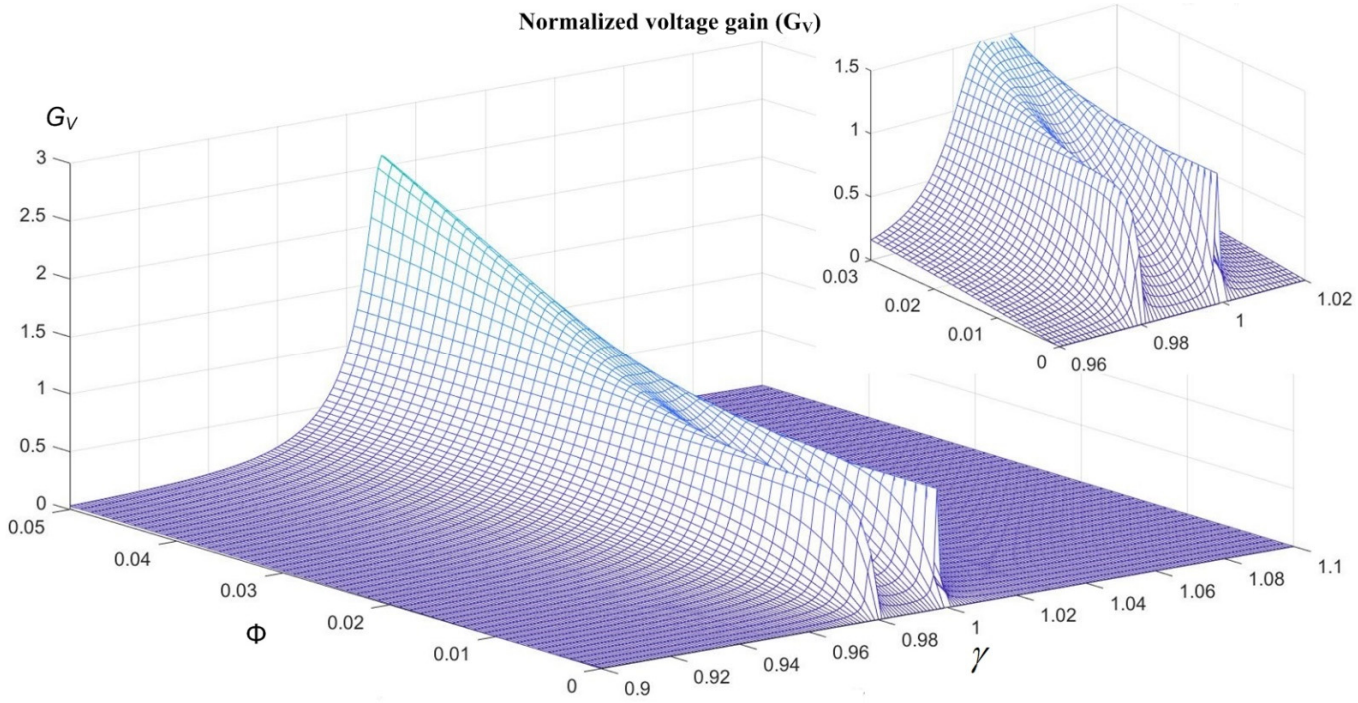

Figure 8. Normalized voltage gain in the function of γ, ϕ, and m = 50.

To achieve a design that meets the resonance condition, it is important to obtain the correct value of ϕ to ensure the correct operation of the system.

4.4. Current Gain Analysis

Analogous to the G_{VT} analysis, the current divisor method and the expressions obtained from the impedance analysis give us the mathematical expression for the total current gain in Expression (22):

$$G_I = \frac{1}{[m+1] - \gamma^2[m+2] + j\phi[m+2]} \quad (22)$$

From Expression (23), the normalized G_I response is obtained as shown in Figure 9; the behavior is similar to that of the normalized impedance graph since the magnitude increases when ϕ is near 0:

$$|G_I| = \frac{1}{\sqrt{([m+1] - \gamma^2[m+2])^2 + \phi^2[m+2]^2}} \quad (23)$$

The design methodology requires an optimal value of ϕ to avoid an abrupt current demand and to stay close to the main resonance peak.

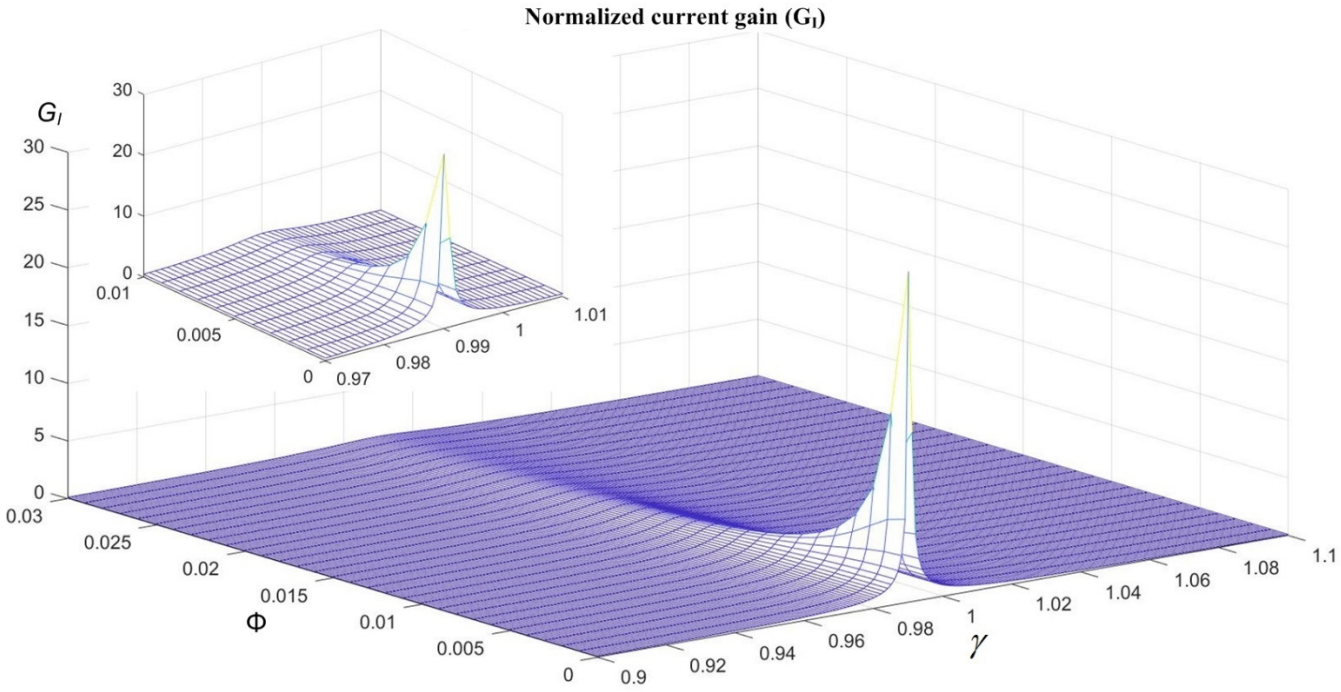

Figure 9. Normalized current gain in the function of γ, ϕ, and m = 50.

4.5. Maximum Energy Transfer

Once the G_V and G_I expressions are found, the optimal load value is calculated to ensure the maximum power transfer from the compensation circuit to the load.

As presented in the previous analyses, the G_V and G_I graphs present opposite behaviors with respect to the variable ϕ; due to this, we propose overlaying both graphs to obtain the optimal values of ϕ and γ to ensure the maximum energy transfer. In Figure 10, the behavior of G_{VT} and G_{IT} is shown for different values of m where it is possible to obtain the particular values of ϕ and γ.

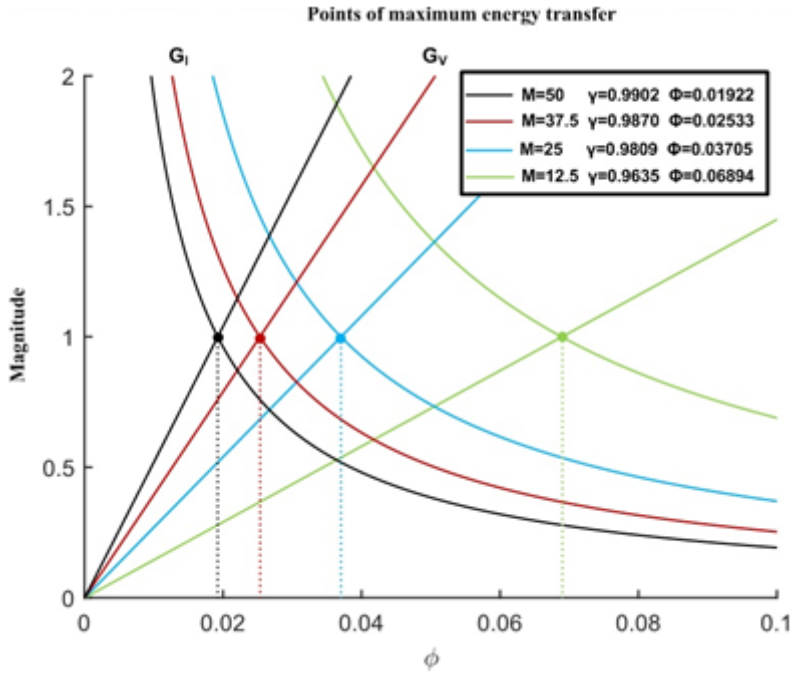

Figure 10. Points of maximum energy transfer.

In Figure 11, the behavior of G_V and G_I is shown at frequency variations for different values of m. The multi-resonance phenomenon can be observed: when $f_{operation}$ moves away from $f_{resonance}$, the second resonance peak moves away from the desired resonance frequency and G_{IT} decreases; this behavior is always present for different values of m. To ensure the maximum energy transfer, the value of γ for a given m must be calculated.

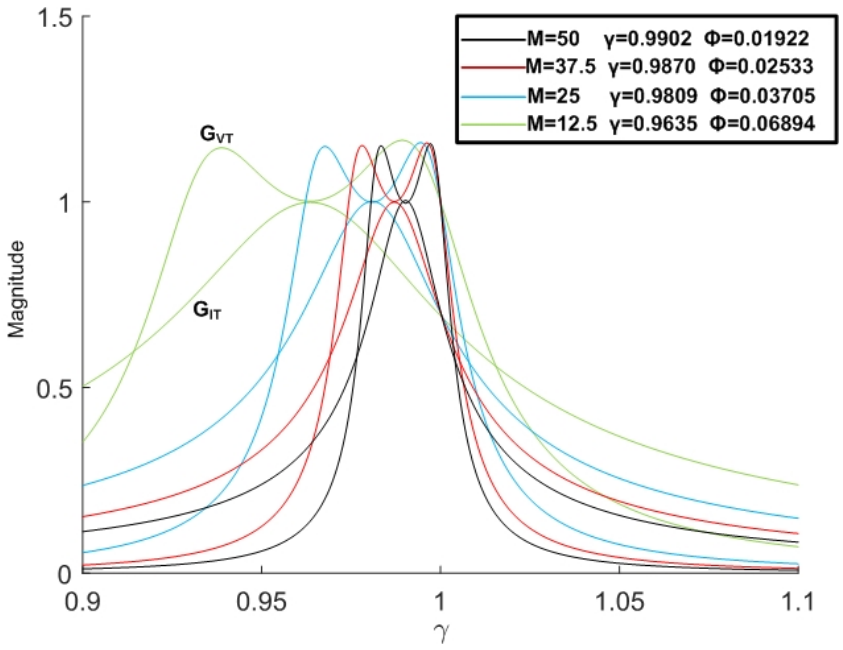

Figure 11. Compensation circuit behavior for frequency variations.

To obtain the load, the cut-off frequency definition is used as:

$$f_{cut\text{-}off\text{-}RC} = \frac{1}{2\pi \cdot R \cdot C} \tag{24}$$

Solving $f_{cut\text{-}off\text{-}RC}$ from the ϕ definition and substituting into Expression (24), C is obtained according to:

$$C = \frac{\phi}{2\pi R f_{operation}} \tag{25}$$

Using Expression (25), and the parameter $f_{operation}$ obtained in Table 1 and in the definition of γ, the parallel capacitance values C_1 and C_2, and the coupling capacitances that ensure maximum energy transfer can be calculated.

5. Design Methodology

According to the expressions obtained for Z_T, G_{VT}, and G_{IT}, a design methodology for calculating the reactive and optimal load components is proposed. The design methodology can be summarized in ten steps:

1. The output power (P_o) is defined;
2. The output load is determined by using the power, voltage, and current in the load (P_o, V_o, and I_o);
3. The optimal capacitor ratio, m, is determined;
4. Optimal values of ϕ and γ are obtained from Figure 10 and Table 1, respectively;
5. The resonance frequency is determined;
6. The operation frequency is obtained according to $f_{operation} = \gamma f_{resonance}$;
7. R_{eq} is obtained with $R_{eq} = \frac{8R_L}{\pi^2 \eta_{rect}}$;
8. The value of the parallel capacitance is estimated with Expression (25): $C = \frac{\phi}{2\pi R f_{operation}}$;

9. The values of the equivalent capacitance (C_{eq}) and the coupling capacitors are obtained with $C_{eq} = \frac{C}{m}$ and $C_{p1} = C_{p2} = 2C_{eq}$;
10. Inductor L is calculated with the resonance frequency of Expression (1).

To validate the design methodology, the multi-resonant circuit values were calculated using the parameters shown in Table 2. Three case studies were considered at different power values. These cases allow validation of the proposed design methodology for different power consumption scenarios.

Table 2. Modified Z-tank values for output power 50 W, 200 W, and 1 kW, considering m = 50, γ = 0.9902, ϕ = 0.0192, $f_{resonance}$ = 1MHz, and $f_{operation}$ = 990.2 kHz.

Output Power = 50 W	**Output Power = 200 W**	**Output Power = 1 kW**
V_s **= 45 V,** R **= 40.5 Ω**	V_s **= 100 V,** R **= 50 Ω**	V_s **= 180 V,** R **= 32.4 Ω**
$R_{eq} = \frac{8R}{\pi^2\eta_{rect}} \approx 33.7\ \Omega$	$R_{eq} = \frac{8R}{\pi^2\eta_{rect}} \approx 41.1\ \Omega$	$R_{eq} = \frac{8R}{\pi^2\eta_{rect}} \approx 26.6\ \Omega$
$C = \frac{\phi}{2\pi R_{eq}\gamma} = 91.67$ pF	$C = \frac{\phi}{2\pi R_{eq}\gamma} = 75.16$ pF	$C = \frac{\phi}{2\pi R_{eq}\gamma} = 116.13$ pF
$r_C = 0.05\ \Omega$	$r_C = 0.05\ \Omega$	$r_C = 0.05\ \Omega$
$C_{p1} = C_{p2} = \frac{2C}{m} = 3.67$ pF	$C_{p1} = C_{p2} = \frac{2C}{m} = 3$ pF	$C_{p1} = C_{p2} = \frac{2C}{m} = 4.65$ pF
$r_{Cp1} = r_{Cp1} = 30\ \Omega$	$r_{Cp1} = r_{Cp1} = 30\ \Omega$	$r_{Cp1} = r_{Cp1} = 30\ \Omega$
$L = \frac{1}{(2\pi f_{resonance})^2 C} \approx 276.32\ \mu$H	$L = \frac{1}{(2\pi f_{resonance})^2 C} \approx 337\ \mu$H	$L = \frac{1}{(2\pi f_{resonance})^2 C} \approx 218.12\ \mu$H
$r_L = 0.1\ \Omega$	$r_L = 0.1\ \Omega$	$r_L = 0.1\ \Omega$

To validate the proposed design procedure, a simulation was performed considering frequency and capacitance variations in the circuit operation.

6. Simulation Results

6.1. Frequency Analysis

A frequency analysis of the circuit shown in Figure 12 was performed under different operating frequency conditions to verify that the maximum energy transfer was achieved.

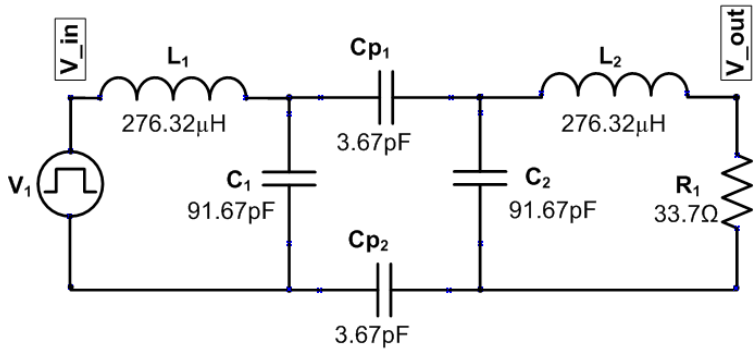

Figure 12. Proposed circuit for frequency simulation.

The behavior of G_V and G_I is shown in Figure 13; it can be noted that the maximum energy transfer takes place at 990.26 kHz, similar to the theoretical expected value. The presence of the multi-resonance phenomenon is also consistent with the theoretical analysis presented in this paper.

To validate that the system is stable under C_p variations, a simulation was performed maintaining the value of all other variables and changing C_p to greater and smaller values than the nominal. Figure 14 shows the behavior of G_V and G_I for C_p values of 2 pF, 4 pF, and 6 pF; it can be corroborated that the compensation circuit does not allow for the frequency to change dramatically from the nominal value.

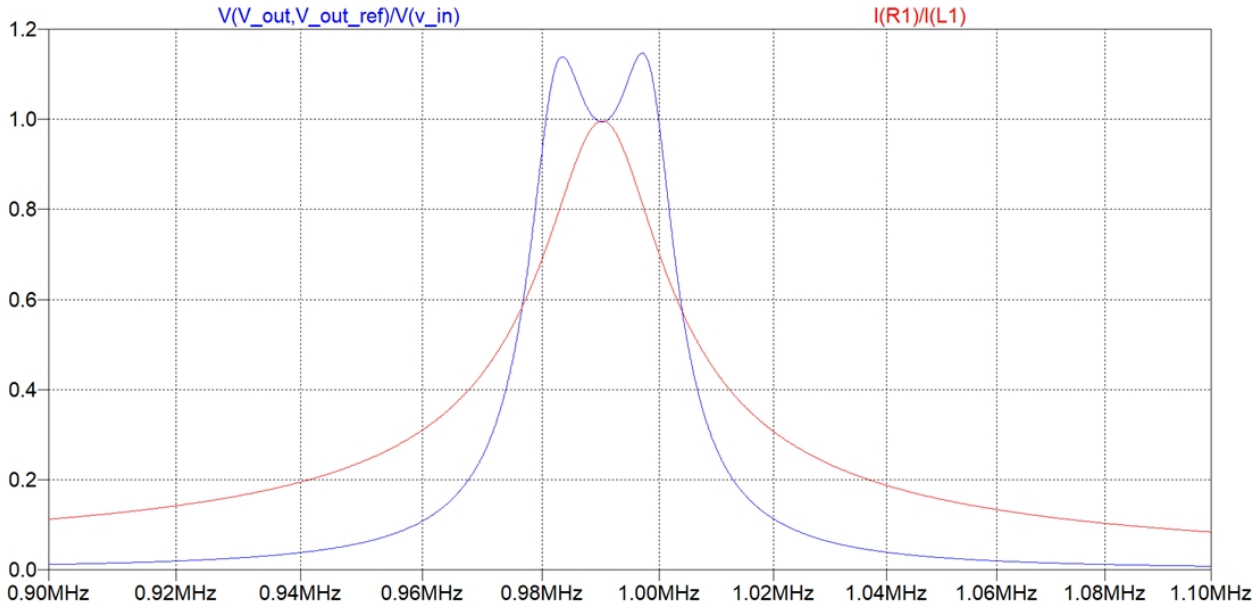

Figure 13. G_V and G_I behavior.

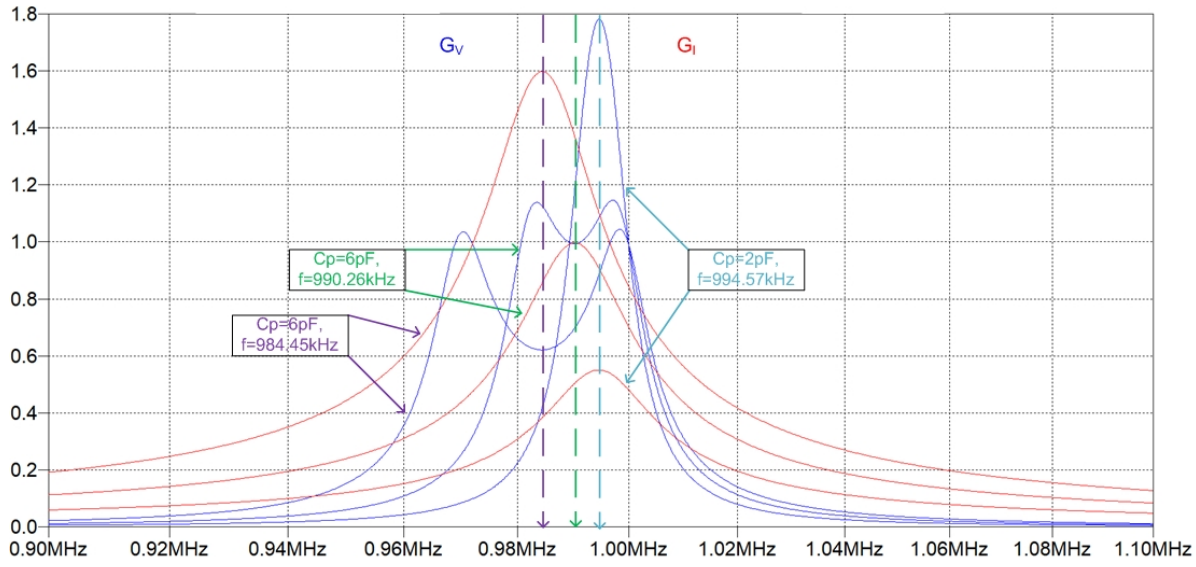

Figure 14. G_V and G_I behavior for different C_p values.

6.2. Time Analysis

To perform a time analysis, the circuit in Figure 15 was simulated. According to [26], the rectifier, filter, and output load can be replaced by an equivalent resistor R_{eq} obtained with:

$$R_{eq} = \frac{8 \cdot R_L}{\pi^2 \cdot \eta_{rect}} \tag{26}$$

$$\eta_{rect} = \frac{1}{1 + \frac{v_f}{V_o}} \tag{27}$$

where η_{rect} is the rectifier efficiency and is calculated with Expression (27), v_f is the forward diode voltage, and V_o is the output voltage. For all the case studies, the circuit used is shown in Figure 15.

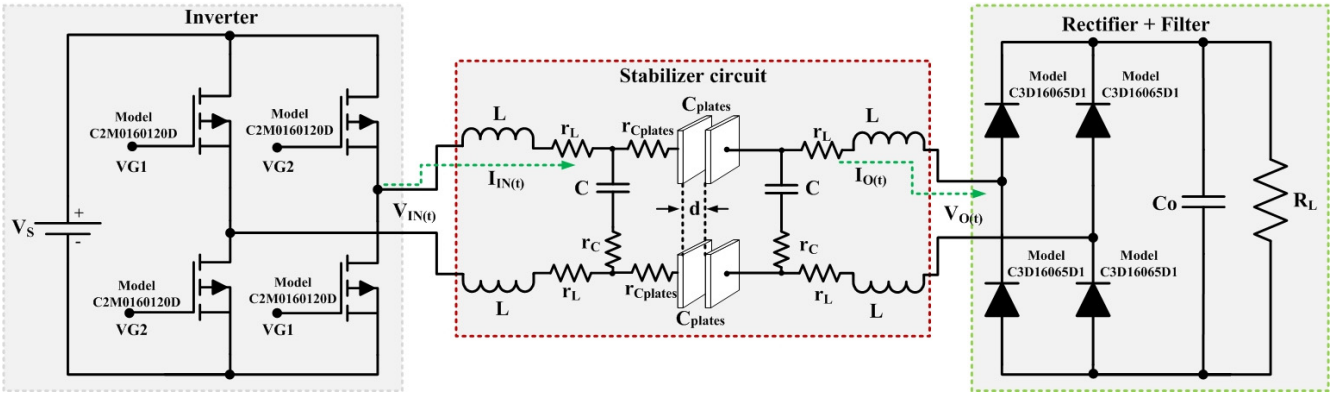

Figure 15. Complete circuit diagram.

6.2.1. Case Study: P_o = 50 W

With the parameters obtained in the design methodology and the data shown in Table 2 for P_o = 50 W, a simulation was performed to obtain the input and output voltage and current waveforms in the multi-resonant circuit; the main results are shown in Figure 16.

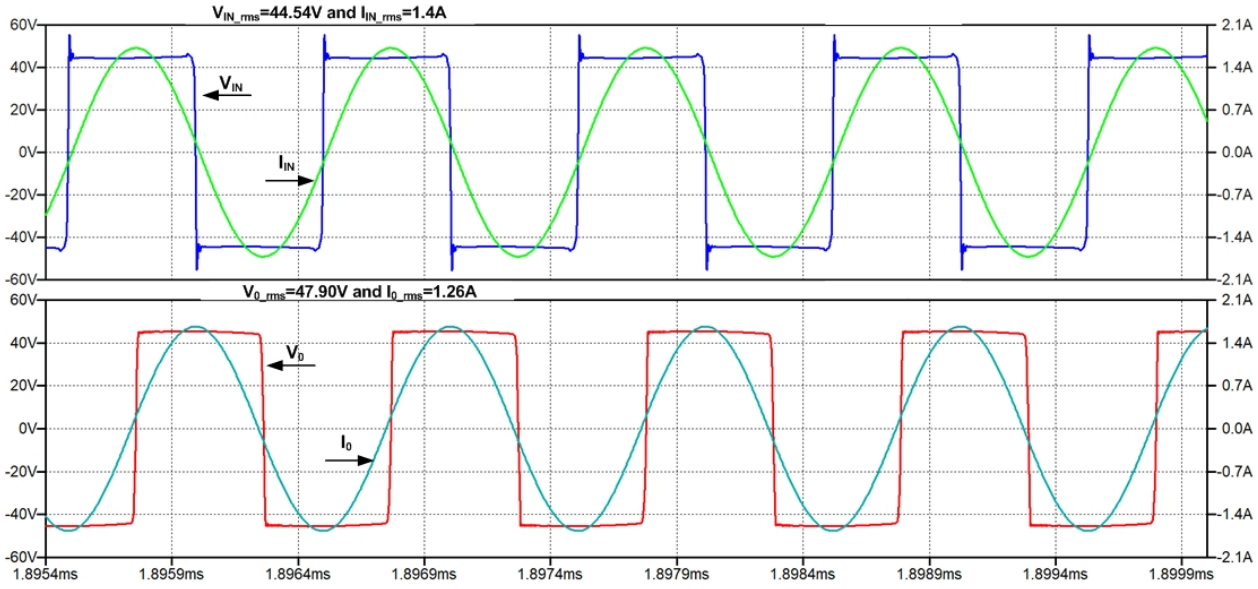

Figure 16. Input voltage (red), output voltage (blue), input current (red), and output current (blue) for P_o = 50 W.

In Figure 16, an output voltage of 47.90 V_{rms} is obtained for an input voltage of 44.54 V_{rms}, where G_V = 1.07 with input and output currents of 1.4 A and 1.26 A, respectively, obtaining G_I = 0.9. From the same figure, it can be seen that the voltage–current mismatch is very close to 0, which indicates that the stabilization circuit operates in resonance. With the values V_{in}, V_o, I_{in}, and I_o the input and output impedances are calculated to determine the multi-resonant circuit efficiency:

$$Z_{in} = \frac{V_{IN}}{I_{IN}} = \frac{44.54\ \text{V}}{1.4\ \text{A}} = 31.81\ \Omega \tag{28}$$

$$Z_{out} = \frac{V_o}{I_o} = \frac{47.90\ \text{V}}{1.26\ \text{A}} = 38.01\ \Omega \tag{29}$$

$$\eta = \frac{(47.90\ \text{V})(1.26\ \text{A})}{(44.54\ \text{V})(1.4\ \text{A})} \times 100\% = 96.78\% \tag{30}$$

The level of efficiency obtained corroborates the compensation circuit's capacity for maximum energy transfer; this demonstrates the validity of the proposed design methodology. Figure 17 shows the value of the current and voltage at the load. The power developed is 51.18 W.

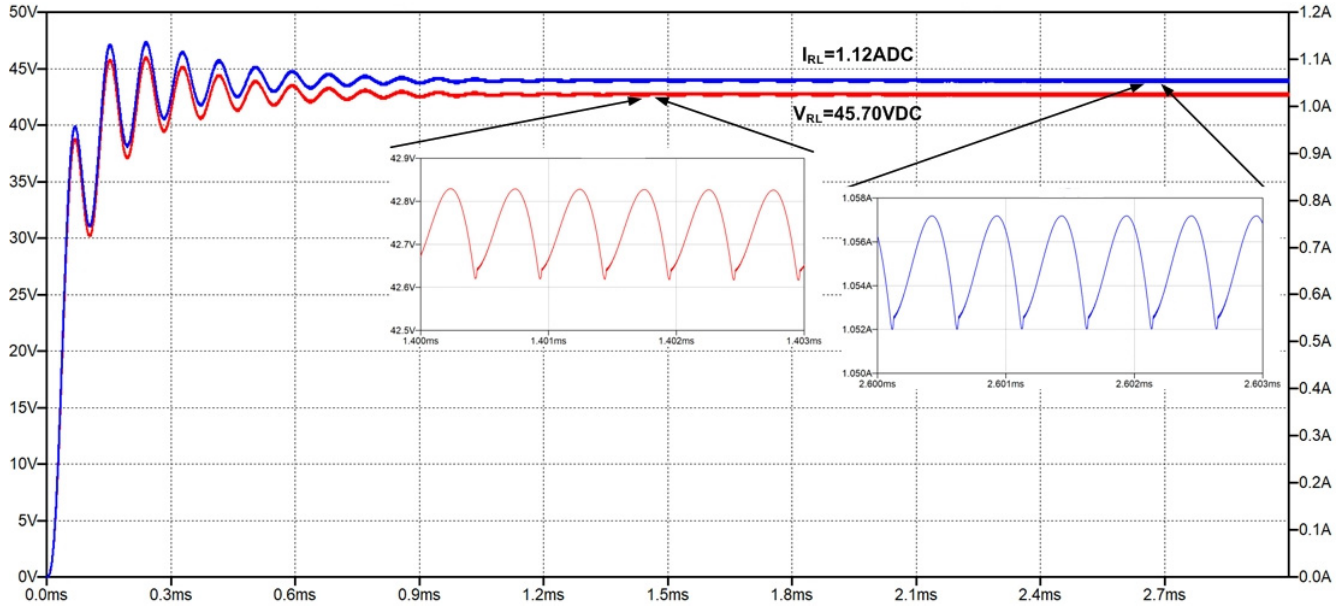

Figure 17. Voltage (red) and current (blue) waveforms at the load.

6.2.2. Case Study: P_o = 200 W

A simulation was performed to obtain the input and output voltage and current waveforms in the multi-resonant circuit with the data presented in Table 2 for P_o = 200 W; the results are shown in Figure 18.

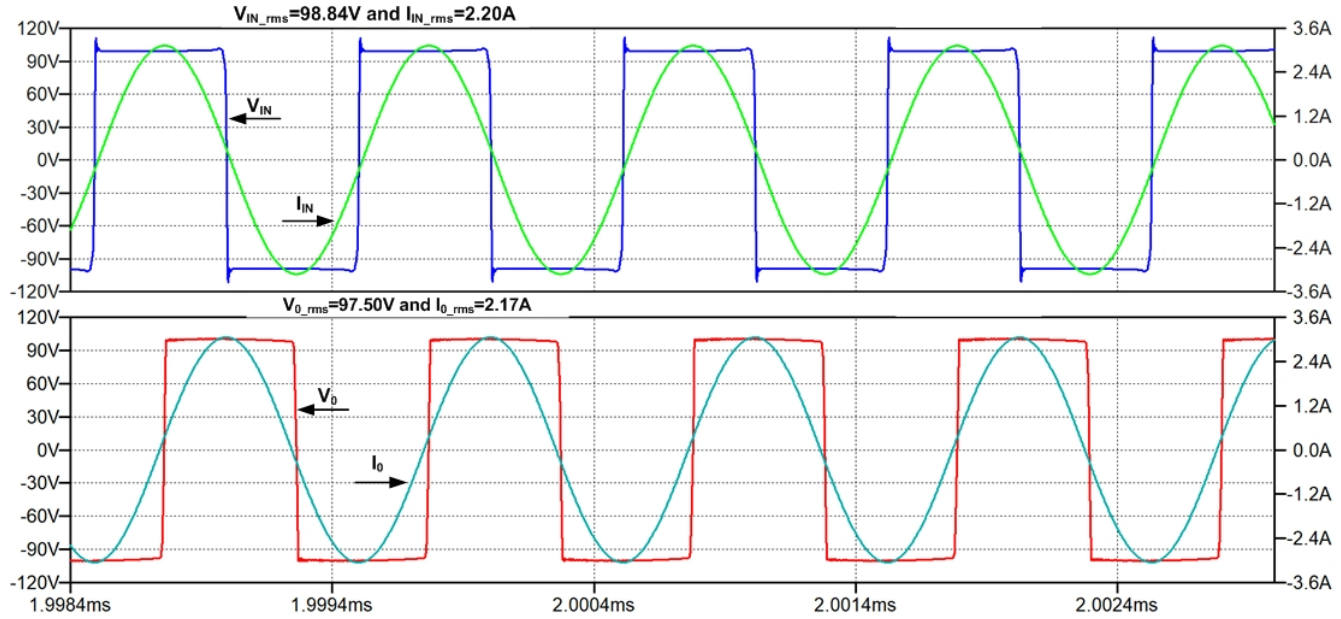

Figure 18. Input voltage (blue), output voltage (red), input current (green), and output current (blue), P_o = 200 W.

In Figure 18, an output voltage of 97.5 V_{rms} is obtained for an input voltage of 98.44 V_{rms}, where G_V = 0.98 with input and output currents of 2.2 A and 2.17 A, respectively,

obtaining G_I = 0.98. For this power scaling, operation is maintained at resonance since the voltage–current phase shift is close to 0. With the values V_{in}, V_o, I_{in}, and I_o, the input and output impedances are calculated to determine the multi-resonant circuit efficiency:

$$Z_{in} = \frac{V_{IN}}{I_{IN}} = \frac{98.84\ \text{V}}{2.2\ \text{A}} = 44.92\ \Omega \tag{31}$$

$$Z_{out} = \frac{V_o}{I_o} = \frac{97.5\ \text{V}}{2.17\ \text{A}} = 44.93\ \Omega \tag{32}$$

$$\eta = \frac{(97.5\ \text{V})(2.17\ \text{A})}{(98.44\ \text{V})(2.2\ \text{A})} \times 100\% = 97.69\% \tag{33}$$

The efficiency obtained corroborates the compensation circuit's capacity for maximum energy transfer and validates its application in a capacitive energy transfer topology with scaling in power. Figure 19 shows the current and voltage at the load. The power developed is 182.73 W.

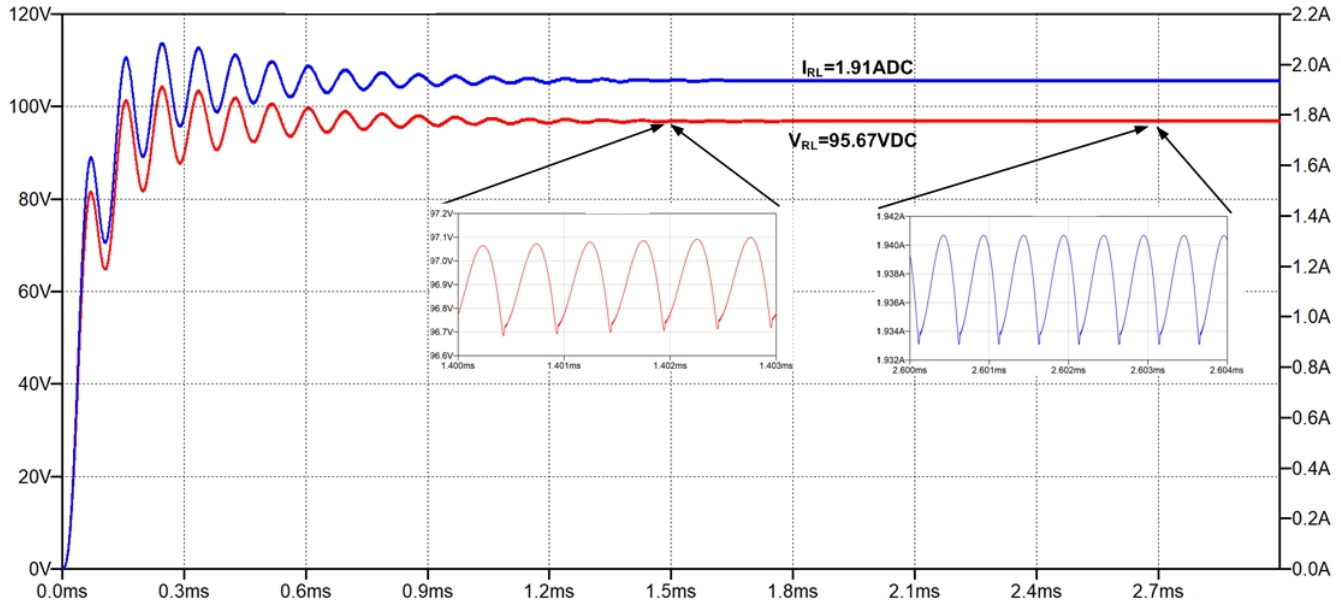

Figure 19. Voltage V_{RL} = 95.67 VDC(red) and current I_{RL} = 1.91 ADC (blue) waveforms at the load.

6.2.3. Case Study: P_o = 1 kW

A simulation was performed to obtain the input and output voltage and current waveforms in the multi-resonant circuit with the data shown in Table 2 for P_o = 1 kW. The results are shown in Figure 20.

In Figure 20, an output voltage of 171.65 V_{rms} is obtained for an input voltage of 176.65 V_{rms}, where G_V = 0.97 with input and output currents of 6.05 A and 5.98 A, respectively, obtaining G_I = 0.988. With the values V_{in}, V_o, I_{in}, and I_o, the input and output impedances are calculated to determine the multi-resonant circuit efficiency:

$$Z_{in} = \frac{V_{IN}}{I_{IN}} = \frac{176.65\ \text{V}}{6.05\ \text{A}} = 29.19\ \Omega \tag{34}$$

$$Z_{out} = \frac{V_o}{I_o} = \frac{171.65\ \text{V}}{5.98\ \text{A}} = 28.70\ \Omega \tag{35}$$

$$\eta = \frac{(171.65\ \text{V})(5.98\ \text{A})}{(176.65\ \text{V})(5.98\ \text{A})} \times 100\% = 96.04\% \tag{36}$$

The efficiency obtained corroborates the compensation circuit's capacity for maximum energy transfer and validates its application in a capacitive energy transfer topology with

scaling in power. Figure 21 shows current and voltage at the load. The power developed is 910.54 W.

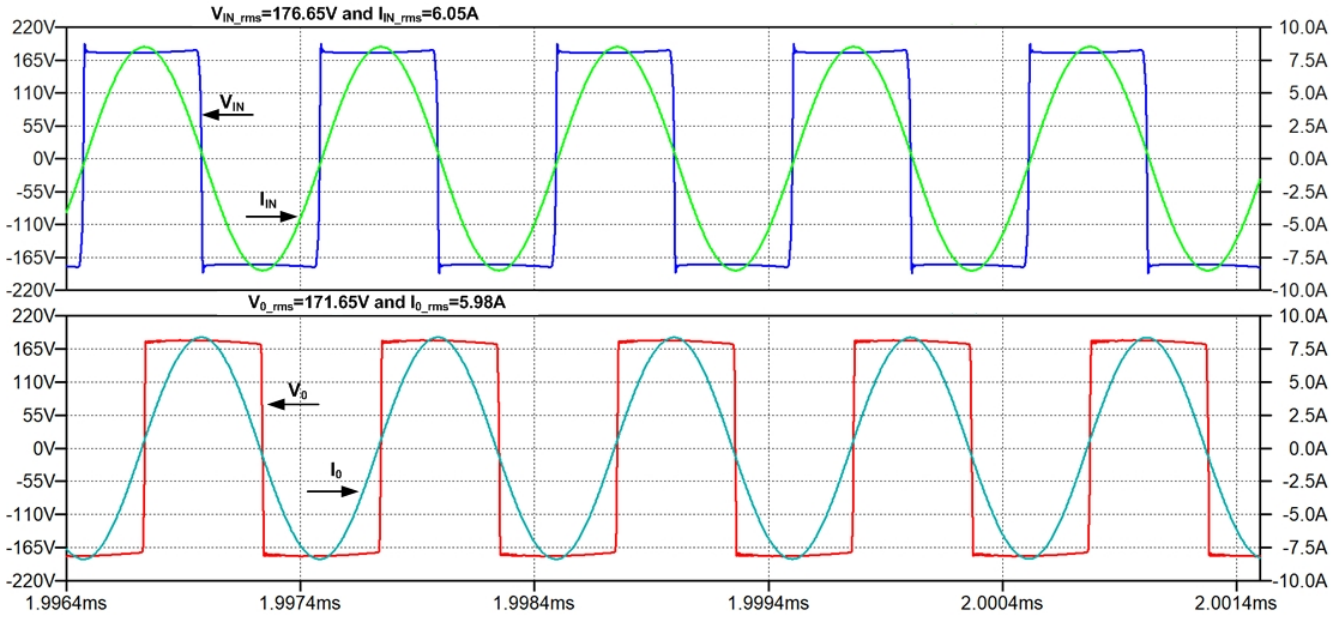

Figure 20. Input voltage (blue), output voltage (blue), input current (red), and output current (green), P_o = 1 kW.

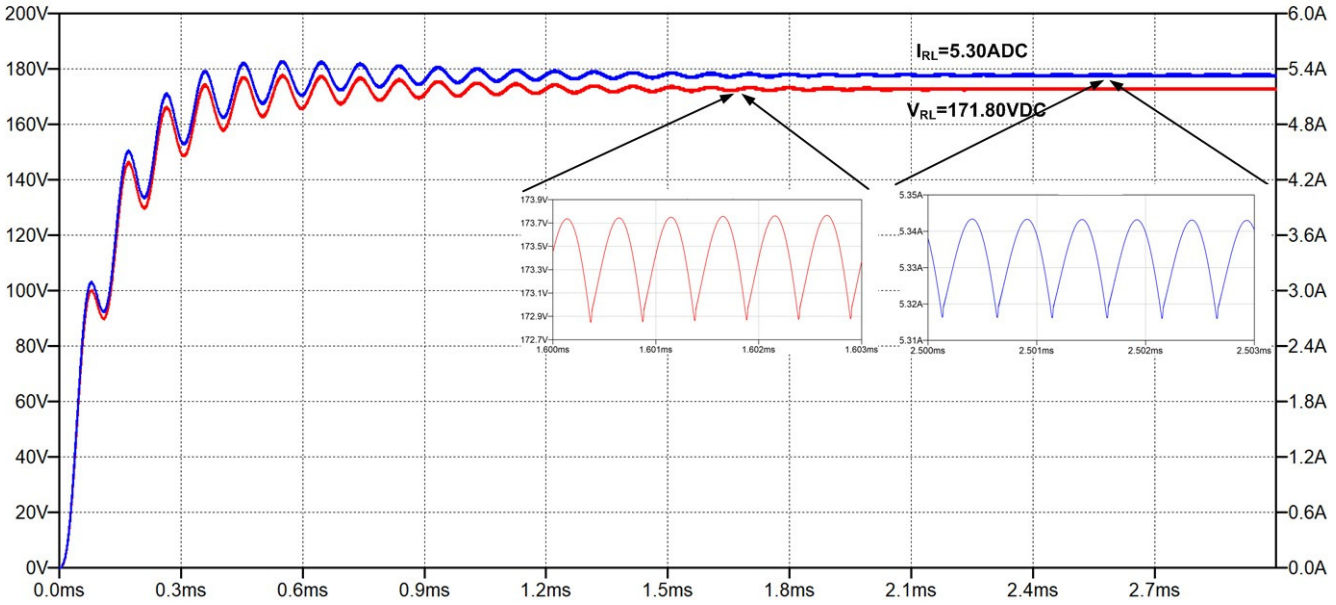

Figure 21. Voltage V_{RL} = 171.80 VDC (red) and current I_{RL} = 5.30 ADC (blue) waveforms at the load.

A comparison between the simulation results for the proposed converter and similar topologies, Refs. [8,27–32] is summarized in Table 3. The proposed converter provides the highest efficiency, and the number of energy storage elements is similar to that of the converters proposed in [31,32]. The high switching frequency operation (1 MHz) is a factor that may reduce the dimensions of the prototype.

Table 3. A comparison between the simulation results for the proposed converter and similar topologies.

Parameter	Proposed	[8]	[27]	[28]	[29]	[30]	[31]	[32]
Output power	1 kW	280 W to 380 W	2.84 kW	3.33 W	1.88 kW	350 W	1.5 kW	160 W
Efficiency	96.04%	87%	94.45%	83%	85.87%	74.1%	85.5%	88.2%
Input voltage	180 V	80 V	310 V	20 V	270 V	100 V	200 V–300 V	140 V–340 V
Output voltage	171.80 V	-	90 V	12.92 V	270 V	132 V	125 V	180 V
Inductors	2	5	4	3	4	2	3	2
Capacitors	3	5	4	5	3	6	3	2
Switching frequency	990 kHz	6.78 MHz	1 MHz	1 MHz	1 MHz	1 MHz	1 MHz	83 kHz
Capacitance of the couplers	4.65 pF	4.62 nF to 8.82 nF	96.1 pF	250 pF	380.9 pF	134 pF	380 pF	2.5 nF

7. Future Work

Future work involves the development of an experimental prototype to validate the design methodology and the efficiency of the entire system. To reach the targeted power density per plate area, we will work with plate capacitance arrays, which will enable us to increase the transmitted power and the apply it directly to the battery charge.

8. Conclusions

The main contribution of this paper is the development of a design methodology for a modified multi-resonant Z-tank circuit that yields design equations for developing a capacitive coupling that can achieve resonance frequency stability despite capacitive coupling changes, for example, distance changes between capacitive plates. In addition, this paper allows us to determine the minimum value of C/C_{eq} and its impact on the proposed design. The methodology establishes the optimal operating frequency and the values of reactive elements necessary to ensure the maximum energy transfer.

Simulation results showed a compensation circuit efficiency of more than 90% with a Total Harmonic Distortion of 0.25%, which is considered sufficient for capacitive wireless transmission applications. To validate the proposed methodology, simulations were carried out at different power values, and the results obtained validated the objective of operating at maximum energy transfer. The multi-resonance phenomenon exhibited by this type of circuit and its dependence on the parameters of normalized frequency and normalized cut-off frequency were also validated.

Finally, the phase shift that occurs between the voltage and the current in both input and output was close to 0, which validated the correct operation at resonant frequency.

Author Contributions: Conceptualization, E.S.E.-E., L.H.-G. and J.C.S.-G.; methodology, L.H.-G., J.R.-H. and J.C.S.-G.; software, E.S.E.-E. and J.R.-H.; validation, E.S.E.-E. and L.H.-G.; formal analysis, E.S.E.-E., L.H.-G., J.C.S.-G. and J.R.-H.; investigation, E.S.E.-E., D.C., O.U.J.-S. and M.P.-S.; resources, J.R.-H., D.C., O.U.J.-S. and M.P.-S.; data curation, D.C., O.U.J.-S. and M.P.-S.; writing—original draft preparation, E.S.E.-E., L.H.-G. and J.C.S.-G.; writing—review and editing, D.C. and M.P.-S.; visualization, J.C.S.-G., J.R.-H. and O.U.J.-S.; supervision, L.H.-G.; project administration, L.H.-G. and J.C.S.-G.; funding acquisition, L.H.-G. All authors have read and agreed to the published version of the manuscript.

Funding: This research was funded by Instituto Politécnico Nacional through the SIP-20210853 Project.

Institutional Review Board Statement: Not applicable.

Informed Consent Statement: Not applicable.

Data Availability Statement: Not applicable.

Acknowledgments: The authors are grateful to the Instituto Politécnico Nacional (IPN) for their encouragement and kind economic support to realize the research project.

Conflicts of Interest: The authors declare no conflict of interest.

References

1. Kuo, R.C.; Riehl, P.; Satyamoorthy, A.; Plumb, W.; Tustin, P.; Lin, J. A 3D resonant wireless charger for a wearable device and a mobile phone. In Proceedings of the IEEE Wireless Power Transfer Conference, WPTC 2015, Boulder, CO, USA, 13–15 May 2015; pp. 1–3.
2. Zaman, H.U.; Islam, T.; Hasan, K.S.; Antora, R.K. Mobile phone to mobile phone wireless power transfer. In Proceedings of the International Conference on Advances in Electrical Engineering, ICAEE 2015, Dhaka, Bangladesh, 17–19 December 2015; pp. 206–209.
3. Chang, C.K.; Yang, C.L. Inductive 3-coil Wireless power transfer improved by T-type impedance matching for implanted biomedical IC. In Proceedings of the IEEE Wireless Power Transfer Conference, WPTC 2015, Boulder, CO, USA, 13–15 May 2015; pp. 1–4.
4. Ahire, D.B.; Gond, V.J. Wireless power transfer system for biomedical application: A review. In Proceedings of the International Conference on Trends in Electronics and Informatics, ICEI 2017, Tirunelveli, India, 11–12 May 2017; pp. 135–140.
5. Li, S.; Mi, C.C. Wireless Power Transfer for Electric Vehicle Applications. *IEEE J. Emerg. Sel. Topics Power Electron.* **2015**, *3*, 4–17.
6. Miller, J.M.; Onar, O.C.; Chinthavali, M. Primary-Side Power Flow Control of Wireless Power Transfer for Electric Vehicle Charging. *IEEE J. Emerg. Sel. Topics Power Electron.* **2015**, *3*, 147–162. [CrossRef]
7. Mohamed, A.A.S.; Lashway, C.R.; Mohammed, O. Modeling and Feasibility Analysis of Quasi-Dynamic WPT System for EV Applications. *IEEE Trans. Transport. Electrific.* **2017**, *3*, 343–353. [CrossRef]
8. Funato, H.; Kobayashi, H.; Kitabayashi, T. Analysis of transfer power of capacitive power transfer system. In Proceedings of the IEEE 10th International Conference on Power Electronics and Drive Systems, PEDS 2013, Kitakyushu, Japan, 22–25 April 2013; pp. 1015–1020.
9. Mi, C. High efficiency wireless power transfer for EV charging and other applications. In Proceedings of the IEEE Energy Conversion Congress and Exposition, ECCE 2017, Cincinnati, OH, USA, 1–5 October 2017; pp. 1–184.
10. Zhou, W.; Su, Y.; Huang, L.; Qing, X.; Hu, P.A. Wireless Power Transfer across Metal Barrier by Combined Capacitive and Inductive Coupling. *IEEE Trans. Ind. Electron.* **2019**, *66*, 4031–4041. [CrossRef]
11. Zou, L.J.; Hu, A.P. A Contactless Single-Wire CPT (Capacitive Power Transfer) Power Supply for Driving a Variable Message Sign. In Proceedings of the IEEE PELS Workshop on Emerging Technologies: Wireless Power Transfer, Montréal, QC, Canada, 3–7 June 2018; pp. 1–5.
12. Su, Y.; Zhao, Y.; Hu, A.P.; Wang, Z.; Tang, C.; Sun, Y. An F-type Compensated Capacitive Power Transfer System Allowing for Sudden Change of Pick-up. *IEEE J. Emerg. Sel. Topics Power Electron.* **2018**, *7*, 1084–1093. [CrossRef]
13. Lu, F.; Zhang, H.; Hofmann, H.; Mi, C. A Double-Sided LCLC Compensated Capacitive Power Transfer System for Electric Vehicle Charging. *IEEE Trans. Power Electron.* **2015**, *30*, 6011–6014. [CrossRef]
14. Lu, F.; Zhang, H.; Hofmann, H.; Mi, C. A CLLC-compensated high power and large air-gap capacitive power transfer system for electric vehicle charging applications. In Proceedings of the IEEE Applied Power Electronics Conference and Exposition, APEC 2016, Long Beach, CA, USA, 20–24 March 2016; pp. 1721–1725.
15. Zhang, H.; Lu, F.; Hofmann, H.; Liu, W.; Mi, C. Six-Plate Capacitive Coupler to Reduce Electric Field Emission in Large AirGap Capacitive Power Transfer. *IEEE Trans. Power Electron.* **2018**, *33*, 665–675. [CrossRef]
16. Ramos, I.; Afridi, K.; Estrada, J.A.; Popovic, Z. Near-field capacitive wireless power transfer array with external field cancellation. In Proceedings of the IEEE Wireless Power Transfer Conference, WPTC 2016, Aveiro, Portugal, 5–6 May 2016; pp. 1–4.
17. Regensburger, B.; Sinha, S.; Kumar, A.; Vance, J.; Popovic, Z.; Afridi, K.K. Kilowatt-scale large air-gap multi-modular capacitive wireless power transfer system for electric vehicle charging. In Proceedings of the IEEE Applied Power Electronics Conference and Exposition, APEC 2018, San Antonio, TX, USA, 4–8 March 2018; pp. 666–671.
18. Zhang, H.; Lu, F. An Improved Design Methodology of the Double-Sided LC-Compensated CPT System Considering the Inductance Detuning. *IEEE Trans. Power Electron.* **2019**, *34*, 11396–11406. [CrossRef]
19. Naoui, M.; Flah, A.; Alqarni, M. Inductive Power Transmission System for Electric Car Charging Phase: Modeling plus Frequency Analysis. *World Electr. Veh. J.* **2021**, *12*, 1–11.
20. Naoui, M.; Flah, A.; Alqarni, M.; Turky, R.A.; Alamri, B.; Ziad, M.A.; Abdel Aleem, S.H.E. A new wireless charging system for electric vehicles using two receiver coils. *Ain Shams Eng. J.* **2021**, *13*, 1–15.
21. Mai, R.; Luo, B.; Chen, Y.; He, Z. Double-sided CL compensation topology-based component voltage stress optimization method for capacitive power transfer charging system. *IET Power Electron.* **2006**, *11*, 1484–1491.
22. Han, Y.; Perreault, D.J. Analysis and Design of High Efficiency Matching Networks. *IEEE Trans. Power Electron.* **2006**, *21*, 1153–1160. [CrossRef]
23. Lu, F.; Zhang, H.; Hofmann, H.; Mi, C.C. A Double-Sided LC Compensation Circuit for Loosely Coupled Capacitive Power Transfer. *IEEE Trans. Power Electron.* **2018**, *33*, 1633–1643. [CrossRef]

24. Huang, D. Investigation of Topology and Integration for Multi-Element Resonant Converters. Ph.D. Thesis, Virginia Polytechnic Institute, Blacksburg, VA, USA, 2013.
25. Zhang, H.; Lu, F.; Hofmann, H.; Mi, C. A loosely coupled capacitive power transfer system with LC compensation circuit topology. In Proceedings of the IEEE Energy Conversion Congress and Exposition, ECCE 2016, Milwaukee, WI, USA, 18–22 September 2016; pp. 1–5.
26. García, A. Análisis de Una Topología de Red Resonante para su Aplicación en Transmisión de Potencia Inalámbrica. Master's Thesis, Tecnológico Nacional de México, Cuernavaca, México, 2020.
27. Lu, F.; Zhang, H.; Hofmann, H.; Mi, C.C. An Inductive and Capacitive Combined Wireless Power Transfer System with LC-Compensated Topology. *IEEE Trans. Power Electron.* **2016**, *31*, 8471–8482. [CrossRef]
28. Huang, L.; Hu, A.P.; Swain, A.K.; Su, Y. Z-Impedance Compensation for Wireless Power Transfer Based on Electric Field. *IEEE Trans. Power Electron.* **2016**, *31*, 7556–7563. [CrossRef]
29. Zhang, H.; Lu, F.; Hofmann, H.; Liu, W.; Mi, C.C. A Four-Plate Compact Capacitive Coupler Design and LCL-Compensated Topology for Capacitive Power Transfer in Electric Vehicle Charging Application. *IEEE Trans. Power Electron.* **2016**, *31*, 8541–8551.
30. Lu, F.; Zhang, H.; Mi, C. A Two-Plate Capacitive Wireless Power Transfer System for Electric Vehicle Charging Applications. *IEEE Trans. Power Electron.* **2018**, *33*, 964–969. [CrossRef]
31. Vu, V.; Dahidah, M.; Pickert, V.; Phan, V. An Improved LCL-L Compensation Topology for Capacitive Power Transfer in Electric Vehicle Charging. *IEEE Access* **2020**, *8*, 27757–27768. [CrossRef]
32. Truong, C.T.; Choi, S.J. Single-Stage Duty-Controlled Half-Bridge Inverter for Compact Capacitive Power Transfer System. *IEEE Access* **2021**, *9*, 119250–119261. [CrossRef]